Imaging Lung Cancer by Using Chemical Exchange Saturation Transfer MRI With Retrospective Respiration Gating

Kyle M. Jones[1], Carol A. Stuehm[2,3], Charles C. Hsu[4], Phillip H. Kuo[2,3], Mark D. Pagel[2,3], and Edward A. Randtke[2,3]

[1]Department of Biomedical Engineering, University of Arizona, Tucson, AZ; [2]Department of Medical Imaging, University of Arizona, Tucson, AZ; [3]University of Arizona Cancer Center, University of Arizona, Tucson, AZ; and [4]Department of Radiation Oncology, University of Arizona, Tucson, AZ

Corresponding Author:
Mark D. Pagel, PhD
Department of Cancer Systems Imaging, University of Texas MD Anderson Cancer Center, 3SCR.3642 Houston, TX 77054:
E-mail: mdpagel@mdanderson.org

ABSTRACT

Performing chemical exchange saturation transfer (CEST) magnetic resonance imaging (MRI) in lung tissue is difficult because of motion artifacts. We, therefore, developed a CEST MRI acquisition and analysis method that performs retrospective respiration gating. Our method used an acquisition scheme with a short 200-millisecond saturation pulse that can accommodate the timing of the breathing cycle, and with saturation applied at frequencies in 0.03-ppm intervals. The Fourier transform of each image was used to calculate the difference in phase angle between adjacent pixels in the longitudinal direction of the respiratory motion. Additional digital filtering techniques were used to evaluate the breathing cycle, which was used to construct CEST spectra from images during quiescent periods. Results from CEST MRI with and without respiration gating analysis were used to evaluate the asymmetry of the magnetization transfer ratio (MTR_{asym}), a measure of CEST, for an egg white phantom that underwent cyclic motion, in the liver of healthy patients, as well as liver and tumor tissues of patients diagnosed with lung cancer. Retrospective respiration gating analysis produced more precise measurements in all cases with significant motion compared with nongated analysis methods. Finally, a preliminary clinical study with the same respiration-gated CEST MRI method showed a large increase in MTR_{asym} after radiation therapy, a small increase or decrease in MTR_{asym} after chemotherapy, and mixed results with combined chemoradiation therapy. Therefore, our retrospective respiration-gated method can improve CEST MRI evaluations of tumors and organs that are affected by respiratory motion.

INTRODUCTION

Lung cancer is the leading cause of cancer-related death in both men and women in the United States, accounting for 27% of cancer deaths in 2014 (1). Positron emission tomography (PET) with ^{18}F-fluordeoxyglucose (FDG), diffusion-weighted magnetic resonance imaging (DW-MRI), perfusion MRI, and computed tomography (CT) have been used to noninvasively evaluate lung masses (2-5). Each modality has its advantages and disadvantages. For example, PET with FDG is a highly sensitive imaging technique, but FDG uptake is nonspecific to tumors, and areas of inflammation may be falsely identified as tumor tissue. DW-MRI has been shown to be successful in differentiating tumor tissue from peritumoral edema, but its strength in evaluating tumors remains questionable owing to the lack of studies showing pathological correlations. Registration of DW-MRI images to the biopsy site is difficult because of image

distortion caused by magnetic susceptibility artifacts. Perfusion CT and MRI have been shown to distinguish malignant nodules from benign pulmonary nodules with greater specificity than assessments of FDG uptake. However, this result has been shown in only lesion sizes ≥16 mm, thus limiting its use to a fraction of the patient population. Additional techniques are required for evaluating lung tumors with medical imaging.

Chemical exchange saturation transfer (CEST) MRI is an innovative biomedical imaging technique that provides molecular-level information about the tissue microenvironment (6). CEST is achieved by applying a saturation pulse at the resonance frequency of labile protons of endogenous molecules, allowing the saturated protons to exchange to the water pool, and by acquiring an image to monitor a decrease in the water signal due to the exchange of saturated protons. The decrease in the water signal is referred to as CEST contrast, which has been repre-

sented by calculating an MTR_{asym} parameter that evaluates the asymmetry in the CEST spectrum (7). More specifically, MTR_{asym} is the ratio of CEST contrast produced by mobile proteins with longer T2 relaxation time constants, relative to a relayed nuclear Overhauser effect (rNOE) produced by less mobile proteins with shorter T2 relaxation times. Therefore, MTR_{asym} is sensitive to the concentration of the protons being saturated (for both CEST and rNOE effects). MTR_{asym} is also sensitive to the exchange rate of the labile protons on endogenous molecules, which increases with increasing pH (owing to the base-catalyzed processes of chemical exchange with most endogenous molecules), and therefore, MTR_{asym} may be sensitive to changes in tumor metabolism that affect tissue pH.

Amide proton transfer (APT) MRI is a specific type of CEST MRI that involves the exchange between endogenous amide protons from mobile proteins and bulk water. Past studies have shown higher APT contrast in tumor tissue than in normal tissue (8), as well as correlations between APT signal intensity and tumor grade as assessed by means of histopathology (9, 10). Thus, measuring the APT contrast in the tumor tissue could eventually become a noninvasive tumor grading technique for evaluating tumors, which may be beneficial for guiding treatment plans.

Most APT studies have been performed to study cerebral stroke and glioma in the brain. Unlike the brain tissue, the lung is difficult to image with MRI owing to motion that blurs the image of the lung and also causes artifacts in the phase dimension of the image. Some studies in the lung have shown that APT MRI can differentiate malignant from benign tumors (11, 12). Unfortunately, one study was completed in the absence of respiration gating, which decreased the image quality. The other study was completed with murine models where the breathing rate was controlled via a ventilator so that the acquisition portion of the CEST sequence was in sync with the quiescent period of the respiratory cycle. The use of a ventilator during MRI with humans is impractical. A respiration-gated technique is desired to generate high-quality results in the lung in free breathing patients.

Recent studies have extracted the breathing signal from features within the image (13-16). These methods eliminate the need for invasive procedures or devices that monitor breathing rates. Extracting the breathing signal from the image features relies on the translational property of Fourier transform (FT) imaging theory, which states that a geometric shift in the space domain results in a phase shift in the Fourier space (17). We used this property to develop an innovative CEST MRI protocol with retrospective respiratory gating. The goal of our study was to examine the strengths and limitations of respiratory-gated CEST MRI when imaging the lungs of healthy volunteers and patients diagnosed with lung cancer.

METHODOLOGY
MRI Acquisition Protocol
Our previous clinical CEST MRI protocol used a saturation period that was at least 3 seconds in length, followed by an MRI acquisition sequence (18). This saturation period is considerably long to sample multiple stages of a typical breathing cycle, which can be 3 seconds at 20 breaths per minute for patients

with compromised respiratory function due to chronic obstructive pulmonary disease (19). Thus, we shortened the saturation pulse to 200 milliseconds to accommodate our CEST MRI method. This shorter duration allowed us to adequately sample stages of a normal respiratory cycle. However, a 200-millisecond saturation pulse is insufficient to generate a steady-state saturation with a series of saturation frequencies that have an interval >0.3 ppm. We also aimed to ensure that a sufficient number of data points in the CEST spectrum were acquired to distinguish the APT and rNOE in the CEST spectrum after retrospectively removing CEST points not acquired during the quiescent stage of breathing. Thus, we shortened the saturation frequency interval for our CEST MRI method to 0.03-ppm units for the entire CEST spectrum so that frequencies next to the saturation frequency being irradiated would also be partially saturated. In doing so, we hypothesized that the CEST spectrum from our CEST MRI method would be similar to a standard CEST spectrum acquired with steady-state saturation, except for the first few CEST magnetic resonance (MR) images of the series that do not experience steady-state saturation.

Simulations
To address the potential pitfalls of insufficiently achieving a steady-state saturation with our saturation scheme, we simulated CEST spectra with a labile pool at 3.5 ppm and 500 mM by using the Bloch equations modified for chemical exchange (20). CEST spectra were simulated using a continuous-wave, rectangular saturation pulse of 200 milliseconds, followed by a delay of 196 milliseconds to account for CEST decay during Fast Imaging with Steady-state Precession (FISP) acquisition, applied to each saturation frequency one time before incrementing to the next saturation frequency in 0.03-ppm increments. We termed this simulation as the "iteratively pulsed" saturation scheme. CEST spectra were also simulated with a saturation pulse of 200 milliseconds followed by a delay of 196 milliseconds to account for FISP acquisition, and these parameters were applied to the same saturation frequency 1000 times before iterating the saturation frequency. We refer to this simulation as the "stationary pulsed" saturation scheme (21). CEST spectra were also simulated by using a saturation pulse of 3.0 seconds followed by a 196-millisecond delay, applied to each saturation frequency 1 time, termed "standard CEST saturation". The B_1 saturation power was set to 1.0 μT for each saturation pulse. In addition, we repeated simulations with a T1 relaxation time constant of 0.8, 1.4, 2.0, and 3.0 seconds, which are characteristic T1 relaxation times of human tissue at 3 T magnetic field strength (22).

Phantom Studies
A solution of egg whites was prepared in a 200-mL plastic container and placed in a larger 500-mL plastic container that was filled with agar (23). The large plastic container was attached to a customized motion device that oscillated in the direction of the longitudinal axis of the magnet. The motion device was placed with the plastic container inside a 3 T MRI scanner (Magnetom Skyra, Siemens). A standard CEST-FISP MRI protocol with steady-state saturation was acquired with a saturation period of 3 seconds and data points from -7 ppm to $+7$ ppm in 0.2-ppm units (24). Then an iteratively pulsed CEST

MRI protocol was acquired with a saturation period of 200 milliseconds and saturation frequencies from −7 ppm to +7 ppm in 0.03-ppm units. For both CEST-FISP MRI protocols, a continuous wave, rectangular pulse shape at 1.0 μT saturation power was used. Both protocols were performed with the phantom container held stationary and with the phantom container moving. The FISP MR images were acquired in a coronal orientation by means of the following parameters: repetition time (TR), 196 milliseconds; echo time (TE), 0.97 milliseconds; excitation angle, 15°; section thickness, 20 mm; in-plane resolution, 4.7 × 4.7 mm^2; field of view (FOV), 300 mm^2; centric encoding; 25% phase oversampling; average, 1; scan time, 3 minutes. For the scans acquired with the phantom in motion, the phantom container was set to move 3 cm toward the front of the magnet over a 1-second time frame, move 3 cm back to its original position over a 1-second time frame, pause for 3 seconds, and then repeat the process to simulate breathing motion.

Clinical Studies

Three healthy volunteers and 3 patients diagnosed with lung cancer underwent scanning to compare standard CEST MRI vs. our iteratively pulsed CEST MRI method with and without retrospective respiratory gating. Then 4 patients with lung carcinoma or mesothelioma treated with radiation therapy and/or chemotherapy underwent scanning using our iteratively pulsed CEST MRI method with retrospective respiratory gating. These studies were performed with the approval of the Institutional Review Board of the University of Arizona. Images were acquired with the same clinical MRI instrument used for imaging phantoms. A 3-dimensional (3D) T1-weighted gradient-echo acquisition was used to localize the liver and lung. Images were acquired in a coronal orientation using the following parameters: TR, 2.93 milliseconds; TE, 1.23 milliseconds; excitation angle, 9°; section thickness, 3 mm; number of sections, 96; section oversampling factor, 33%; in-plane resolution, 1.5 × 1.5 mm^2; FOV, 420 mm^2; partial k-space of 6/8, with a 3D caipirinha acceleration factor, a factor of 3 in the phase direction, and a factor of 2 in the section direction; linear encoding; average, 1; and scan time, 12 seconds. For patients with cancer, a 2D multisection T2-weighted HASTE acquisition was also used to further localize the tumor. Images were acquired in a coronal orientation by means of the following parameters: TR, 1500 milliseconds; TE, 75 milliseconds; excitation angle, 80°; refocusing angle, 160°; section thickness, 6 mm; number of sections, 35; in-plane resolution, 1.0 × 1.0 mm^2; FOV, 400 mm^2; 2D GRAPPA with a factor of 3; k-space sampling, 5/8; linear encoding; average, 1; and scan time, 54 seconds. This sequence was performed with fat suppression by using spectral attenuated inversion recovery. CEST-FISP MR images were acquired using the same method as the phantom experiment.

Image Processing and Analysis

We segmented the temporal series of CEST spectra on the basis of the quiescent period during expiration of the breathing cycle because the quiescent period would have the most consistent positioning of the liver and tumor (25). To segment the breathing cycles, we selected a region of interest (ROI) around the liver dome because the intersection between the liver dome and the lung has great contrast and the movement of the liver dome is a direct result of inhalation and exhalation. This ROI was selected using the first FISP image and then applied for all FISP images acquired with our iteratively pulsed CEST MRI method.

We obtained the respiration cycle from the CEST MR images. An FT was applied to the ROI in all FISP images to convert the spatial image to k-space (Figure 1, A and B). The pixel at the center of k-space and the adjacent pixel along the longitudinal axis of displacement were selected for analyses. A ratio of the MR signal amplitudes of these 2 pixels was used to determine the difference in the phase angle between the 2 pixels (Figure 1C). We used these 2 pixels because the phase angle differences between these pixels are the most sensitive to respiratory motion (14). Plotting the phase angle difference for each FISP image acquired with respect to time represented the overall motion including the respiratory cycle.

We applied a series of digital filtering techniques to refine the monitored respiratory cycle (Figure 1, D–F). First, we applied an FT to the phase angle difference spectrum and then applied a bandpass filter to retain the frequencies between 0.11 Hz (7 bpm) and 0.48 Hz (29 bpm) because these breath rates between these values correspond to typical respiratory rates (19). Next, we applied an inverse FT to the digitally filtered data to generate a refined respiratory cycle plot. Because we sought to obtain the quiescent period of the breathing cycle, we adjusted the respiratory cycle plot so that the quiescent period was centered at 0 radians.

We identified the quiescent period of the plot by assuming that the respiratory cycle was sinusoidal [equations (1) and (2)].

$$S(\theta) = A \cdot \sin(B + \theta) + S \qquad (1)$$

where A = amplitude, B = phase angle shift, θ = respiratory phase, and S = nonsinusoidal signal

$$S(\theta) = C \cdot \sin(\theta) + D \cdot \cos(\theta) + S \qquad (2)$$

where C and D are the amplitudes of the sine and cosine components, respectively. The values of C, D, and S were determined from the inner product between $\sin(\theta)$ and the respiratory signal, $\cos(\theta)$ and the respiratory signal, and 1 and the respiration signal. Once C and D were determined, the phase shift of the respiratory cycle was found using equation (3). This value was used to re-center the peak of the sinusoid at 0 radians.

$$B = tan\frac{C}{D} \qquad (3)$$

All CEST data points that had an FISP image with a phase angle difference of <1 radian from B were retained in the final CEST spectrum (Figure 1, G and H). This threshold of 1 radian retained ~30% of the images that were used to obtain the final CEST spectrum.

MTR$_{asym}$ Analysis

To adjust for B$_0$ inhomogeneity, the minimum signal of each CEST spectrum was set to 0 ppm. Then, the CEST spectrum was fit with a single Lorentzian line shape conducive to the spectral shape for direct water saturation (26). The fitted offset value for
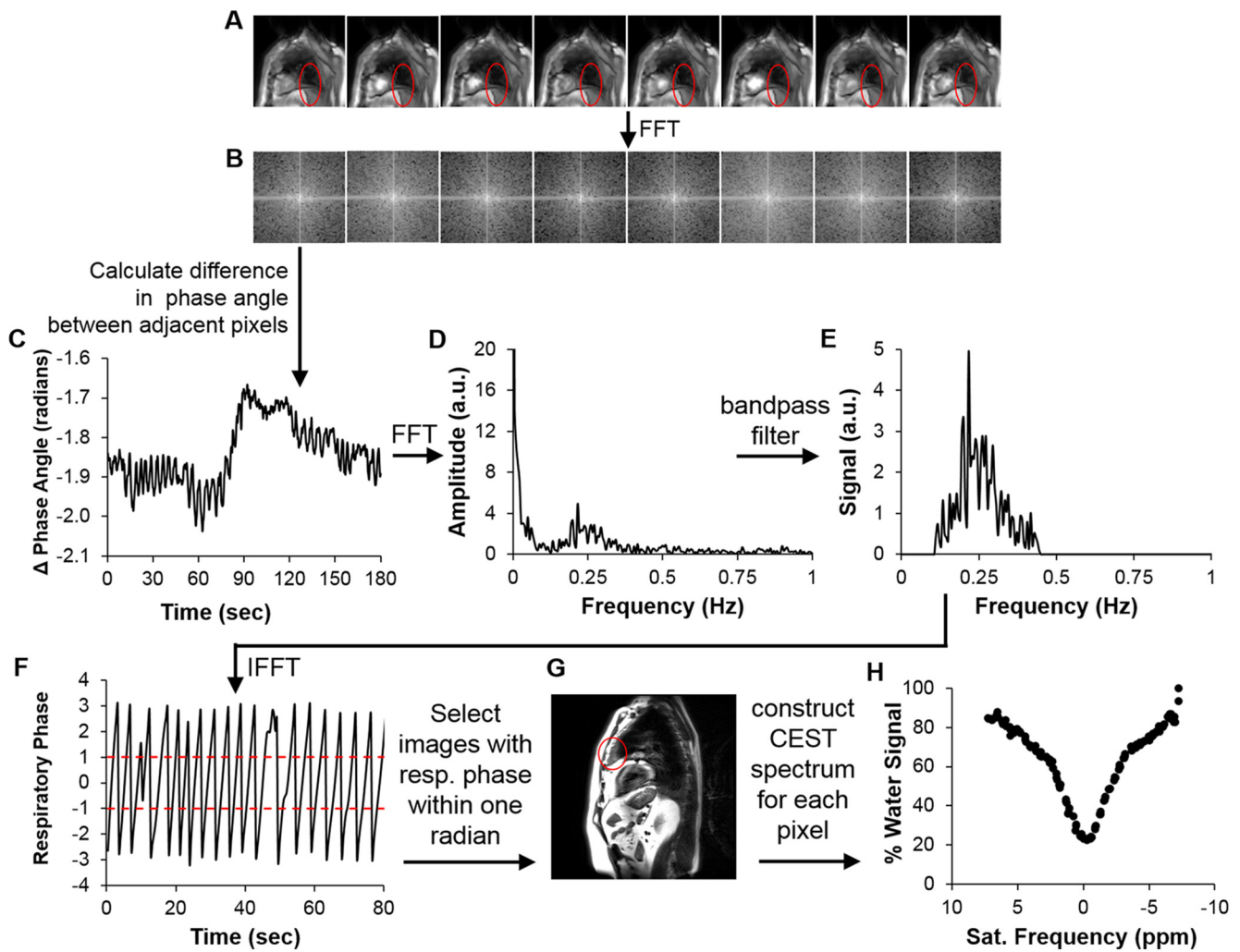
Figure 1. An example of retrospective respiration gating for CEST MRI. A region of interest (ROI) of the diaphragm was selected (red oval) (A). The images of this ROI were Fourier transformed (B). The difference in the phase angle between adjacent pixels in the direction of motion was used to track motion (C). The dynamic respiration profile was obtained by applying a fast Fourier transform (FFT) (D), a bandpass filter (E), and an inverse fast Fourier transform (IFFT) (F). Chemical exchange saturation transfer (CEST) images within 1 radiation of the maximum of each respiratory cycle were selected (G), which were used to construct CEST spectra for each pixel in the ROI (H).

this line shape was used to further adjust the 0-ppm value of the CEST spectrum. To generate an MTR_{asym} value, a straight line was drawn through all points from 2.5 to 4.5 ppm, and the center point of the line was taken as the contrast value for the APT effect (S_{APT}) (27). The same procedure was used for points between −4.5 and −2.5 ppm to generate the contrast value for the rNOE (S_{rNOE}). MTR_{asym} was determined from S_{APT}, S_{rNOE}, and the signal amplitude of the last CEST spectrum data point (S_0; equation (4)) (7).

$$MTR_{asym} = (S_{rNOE} - S_{APT}) / S_0 \qquad (4)$$

In healthy subjects, an ROI was selected around the entire liver, and each pixel within the ROI was analyzed using MTR_{asym} analysis as described above. The same approach was performed for patients diagnosed with lung cancer, except that the ROI for

the tumor was selected by a board-certified radiologist with access to standard-of-care diagnostic CT and/or PET/CT imaging. The standard deviation was calculated from the MTR_{asym} values from all pixels within the ROI.

RESULTS

Simulations of CEST MRI

The simulated CEST spectrum constructed with the iteratively pulsed saturation scheme was identical to the simulated CEST spectrum constructed with stationary pulsed saturation at all T1 times tested (Figure 2). Therefore, iterating the saturation frequency in small 0.03-ppm increments had no effect on the image contrast when using a small 200-millisecond saturation pulse. Both simulations with a 200-millisecond saturation pulse produced less APT contrast at 3.5 ppm than the standard CEST
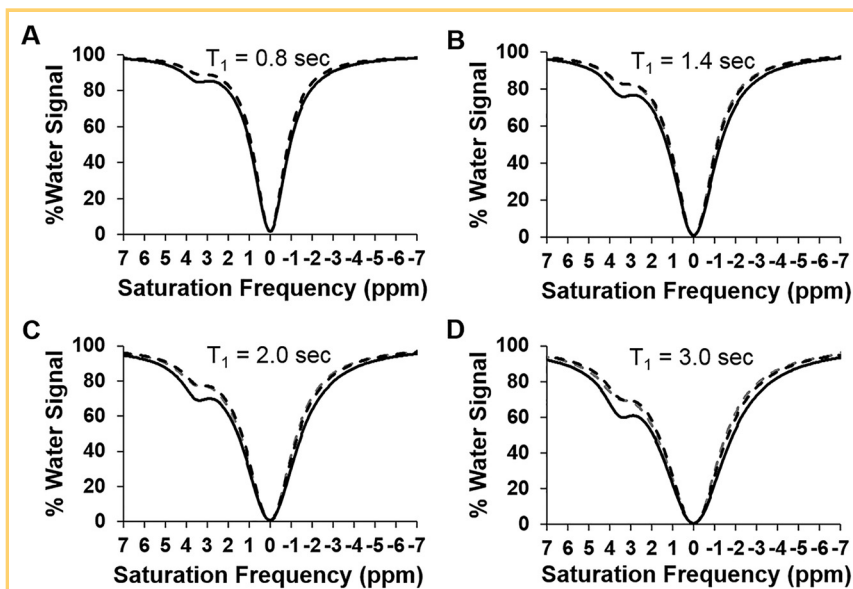
Figure 2. Simulations of CEST spectra with standard CEST saturation (solid black line), stationary pulsed saturation (dashed black line), and iteratively pulsed saturation (dashed gray line) at T1 relaxation times of 0.8 seconds (A), 1.4 seconds (B), 2.0 seconds (C), and 3.0 seconds (D).

MRI pulse sequence with saturation applied for 3.0 seconds. This lower contrast was expected, because interleaving a 196-millisecond delay with the saturation pulses to account for the FISP acquisition sequence lowered the duty cycle of the saturation during the entire CEST MRI protocol.

Phantom Studies

Our studies with phantoms undergoing motion showed that the iteratively pulsed CEST MRI acquisition with retrospective respiration gating analysis generated more precise MTR_{asym} values compared with the standard CEST MRI acquisition method and
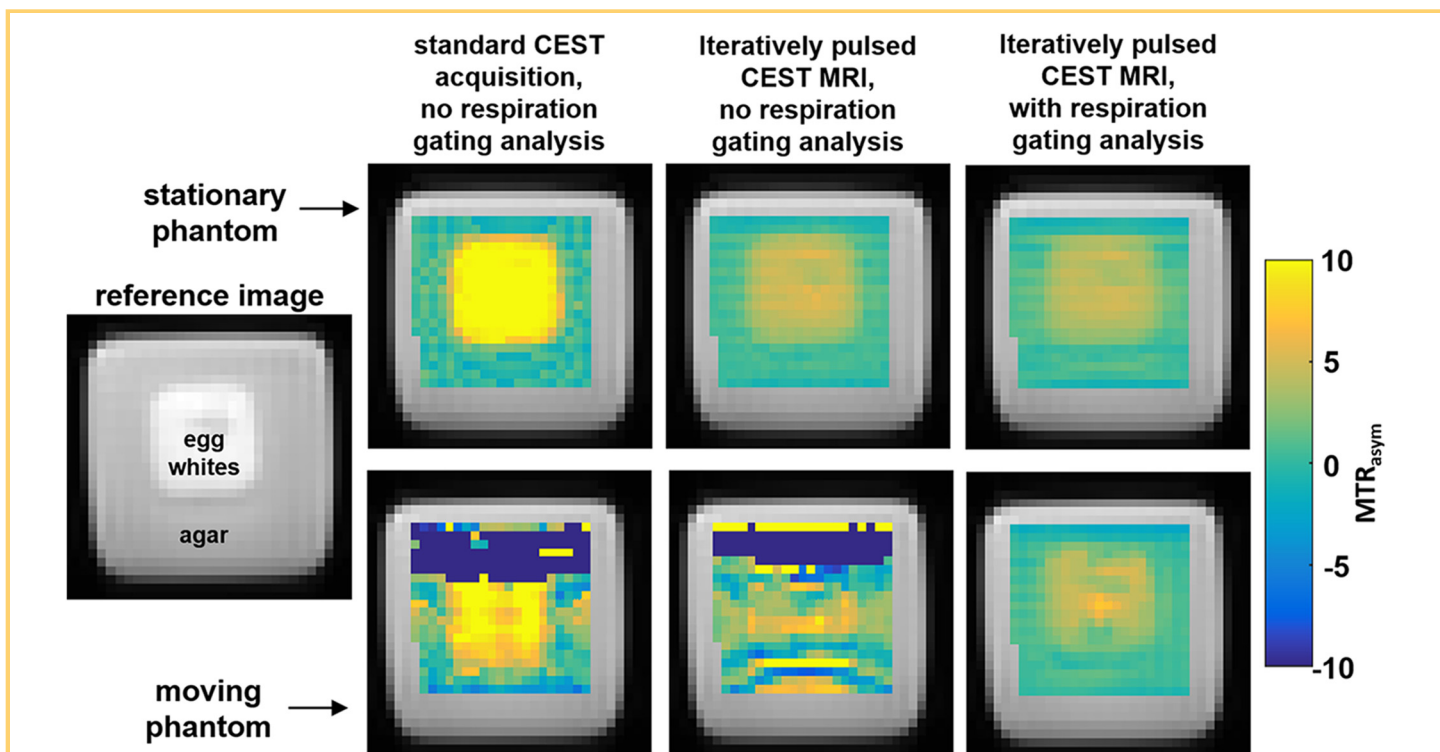

Figure 3. Respiration-gated CEST magnetic resonance imaging (MRI) studies of an egg white phantom. The standard CEST MRI protocol without respiration-gating analysis detected 10% MTR_{asym} in a stationary phantom, whereas the iteratively pulsed CEST MRI protocol with or without respiration gating analysis detected 5% MTR_{asym}. When the phantom was moving in an oscillatory fashion, only the iteratively pulsed CEST MRI protocol with retrospective respiration gating analysis produced a similar MTR_{asym} contrast map relative to results with the stationary phantom.

Table 1. %MTR$_{asym}$ of Phantoms and Patients Diagnosed With Lung Cancer

Phantom or Patient	Phantom Status or Tissue Type	%MTR$_{asym}$ (Mean ± Standard Deviation)		
		Standard CEST MRI	Iteratively Pulsed CEST MRI	
		Without Retrospective Respiration Gating	Without Retrospective Respiration Gating	With Retrospective Respiration Gating
Phantom	Stationary	9.5 ± 2.0	4.1 ± 0.9	3.7 ± 0.8
	Moving	−5.7 ± 21.7	−5.6 ± 15.5	3.4 ± 1.4
Patient 1	Tumor in mediastinum	2.5 ± 1.9	0.1 ± 1.2	1.0 ± 1.4
	Liver	0.8 ± 32.8	−4.3 ± 19.8	−1.8 ± 3.4
Patient 2	Tumor in mediastinum	21 ± 9.2	17.7 ± 8.1	17.0 ± 7.6
	Tumor near collapsed lung	−1.2 ± 10.5	1.3 ± 20.8	−3.1 ± 5.4
	Collapsed lung	−9.7 ± 23.1	3.0 ± 11.2	−1.0 ± 7.9
	Liver	−0.7 ± 6.7	0.8 ± 22.1	2.0 ± 2.8
Patient 3	Tumor above heart	−0.4 ± 1.7	−3.2 ± 27.8	−2.2 ± 2.5
	Liver	−0.7 ± 6.7	0.8 ± 22.1	2.0 ± 2.8

the iteratively pulsed CEST MRI method without retrospective respiration gating (Figure 3; Table 1). The iteratively pulsed CEST MRI acquisition and respiration-gated analysis estimated similar MTR$_{asym}$ values and standard deviations of the pixelwise maps when the phantom box was stationary and when the phantom box was moving. CEST MRI acquisitions without ret-

rospective respiratory gating analysis estimated considerably different MTR$_{asym}$ values and standard deviations when the phantom was held stationary compared with a moving phantom. In addition, the mean MTR$_{asym}$ value with the standard CEST MR acquisition was significantly higher than the mean MTR$_{asym}$ value with the iteratively pulsed CEST acquisition for the stationary
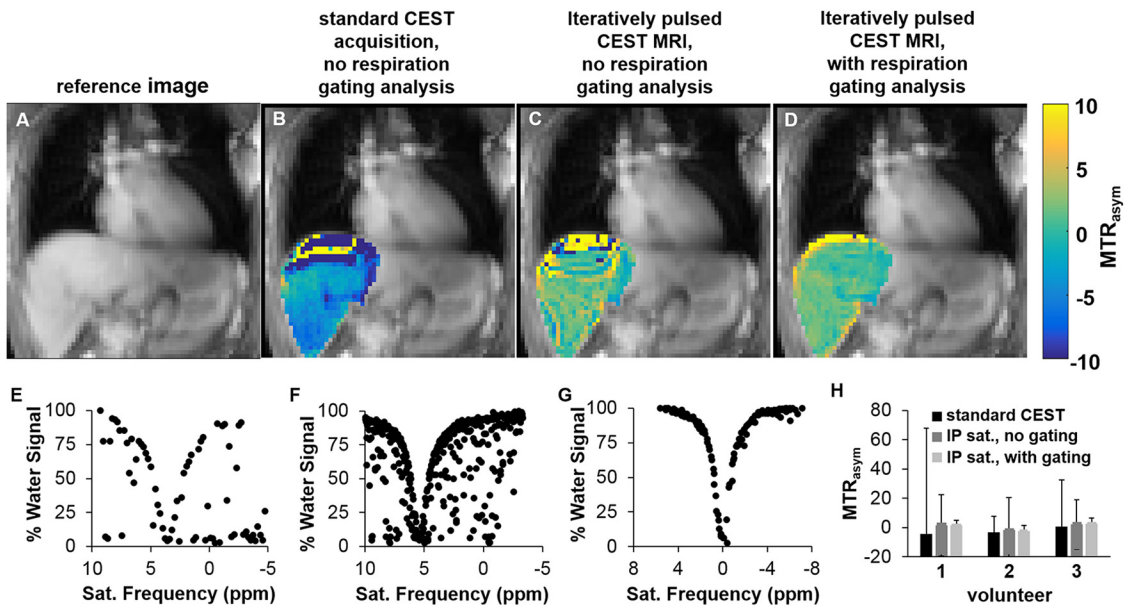

Figure 4. CEST MRI imaging of healthy volunteers. A reference image showed the location of the liver dome (A). When analyzed without retrospective respiration gating, the MTR$_{asym}$ was heterogeneous throughout the liver (B, C). When using the iteratively pulsed CEST MRI protocol with retrospective respiration gating, the results throughout the liver were relatively homogenous (D). CEST spectra of the liver dome are shown with the standard acquisition method (E) and with iteratively pulsed saturation without (F) and with (G) retrospective respiration gating analysis. The average MTR$_{asym}$ values of the liver were similar for the 3 volunteers only when the iteratively pulsed CEST MRI protocol with respiration gating analysis was used (H). Error bars represent the standard deviation of the distributions of pixelwise MTR$_{asym}$ values.
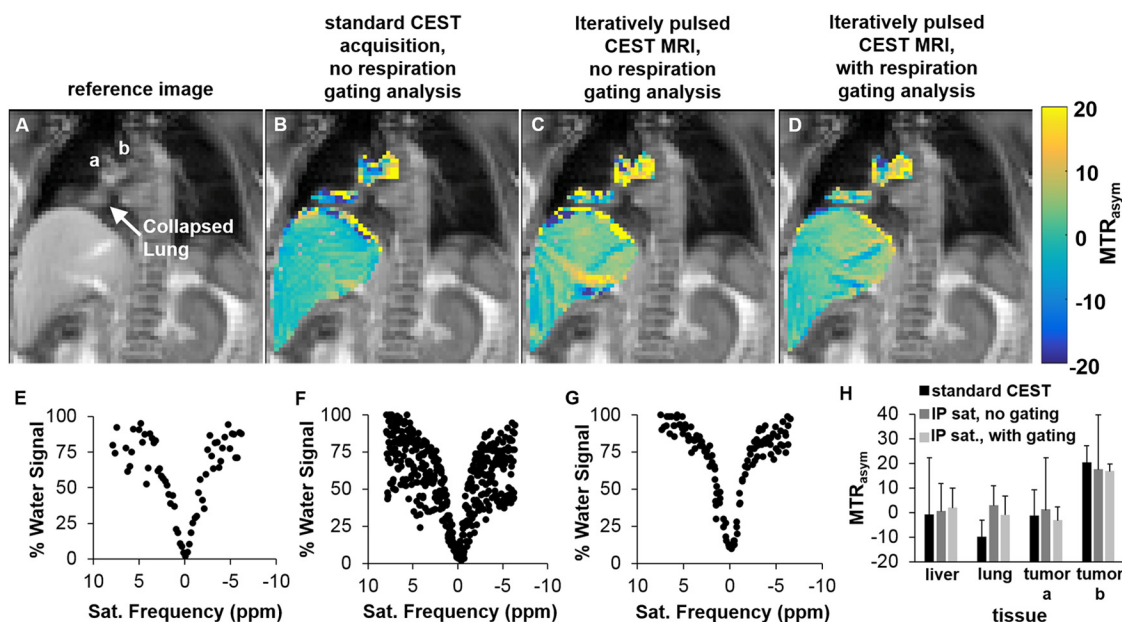
Figure 5. CEST MRI of a patient with lung cancer. A reference image showed the location of 2 tumors (labeled as **a** and **b**), as well as liver and a region of collapsed lung (A). When analyzed without respiration gating analysis, the MTR_{asym} value was heterogeneous throughout all regions (B, C). When using the iteratively pulsed CEST MRI protocol with retrospective respiration gating, the results throughout the liver and collapsed lung tissue were relatively homogenous (D). CEST spectra of tumor **a** are shown with the standard acquisition method (E) and with iteratively pulsed saturation without (F) and with (G) retrospective respiration gating analysis. The average MTR_{asym} values of the 4 tissue regions are shown (H). Error bars represent the standard deviation of the distributions of pixelwise MTR_{asym} values.

phantom. This difference in mean MTR_{asym} values was attributed to the difference in the duty cycle during saturation. This finding agreed with results observed in simulations.

Clinical Studies

Our clinical studies showed that iteratively pulsed CEST MRI acquisition method with retrospective respiratory gating analysis produced more precise MTR_{asym} values compared with CEST MRI acquisition methods without retrospective respiration gating. This improvement in MTR_{asym} measurements was observed for the liver of healthy subjects (Figure 4), as well as the tumor, collapsed lung tissue, and liver of patients diagnosed with lung cancer (Figure 5; Table 1). In the 3 healthy subjects, the standard deviation of the MTR_{asym} values of the pixels of the liver was 3.8%, 3.6%, and 3.9% with our respiration gated analysis method; 72%, 11%, and 32% with the standard CEST MRI acquisition method; and 21%, 22%, and 17% with the iteratively pulsed CEST MRI acquisition without respiration gating. In addition, in the 3 patients diagnosed with lung cancer, the standard deviation of the MTR_{asym} values of the pixels of the liver was less with our respiration gated method than with methods without respiration gating, further showing the superiority of CEST MRI with retrospective respiration gating in the liver.

The locations in the lung varied for the tumors in the 3 patients diagnosed with lung cancer. Tumors that moved significantly with breathing were measured with more precision by using CEST MRI with respiratory gating compared with methods

without respiratory gating. Tumors that experienced only minor lung motion showed comparable results with or without respiration gating (patients 1 and 3).

To perform an exploratory clinical study, 4 patients with lung carcinoma or mesothelioma were imaged with iteratively pulsed, retrospective respiratory-gated CEST MRI before and after treatment with radiation therapy and/or chemotherapy (Figure 6; Table 2). Two patients were scanned before and after radiation therapy alone, and 1 patient was scanned before and after chemotherapy alone. One patient was scanned before and after chemoradiation therapy and then again before and after chemotherapy alone. From these 4 patients, 8 tumor sites were analyzed before and after therapy. The initial MTR_{asym} value varied from -0.27% to 8.18% among the tumors, suggesting a range in mobile protein content and/or pH among the tumors. All 3 tumors that were treated with radiation therapy showed a large increase in the MTR_{asym} value after treatment, indicating an increase in mobile protein content or an increase in tumor pH. All 3 tumors when treated with chemotherapy alone showed a small increase or decrease in MTR_{asym}. One of the 2 tumors treated with chemoradiation showed a large increase in MTR_{asym}, whereas the other tumor treated with chemoradiation showed a small decrease in MTR_{asym}. These results may indicate that CEST MRI is more sensitive to radiation therapy than to chemotherapy. Finally, the increase in MTR_{asym} was related to the initial MTR_{asym} value in 7 of the 8 tumors and treatments studied (Figure 6B), suggesting that the initial MTR_{asym} value may predict the mag-

Figure 6. CEST MRI of patients undergoing treatment. The $\%MTR_{asym}$ increased after treatment for 6 of the 8 tumors that were studied (A). Larger changes were observed following radiation therapy than with chemotherapy. The increase in $\%MTR_{asym}$ was directly related to the $\%MTR_{asym}$ before treatment (B). Circles represent tumors treated with radiation therapy; squares represent tumors treated with chemotherapy; triangles represent tumors treated with chemoradiation therapy.
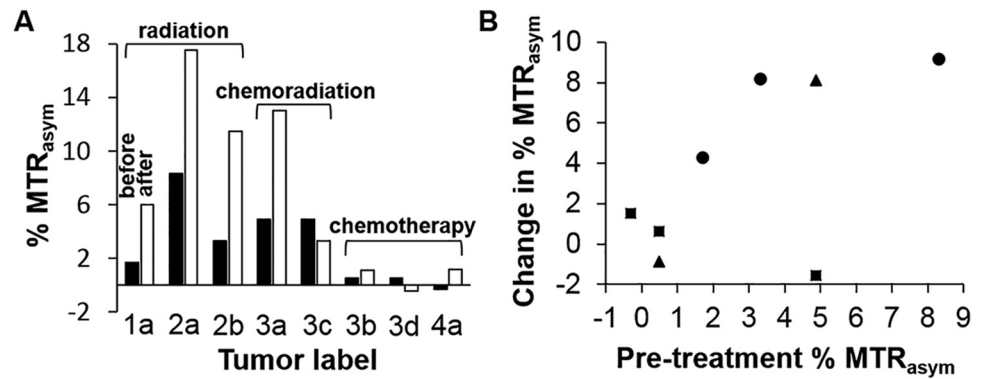
nitude of the treatment-induced change in CEST MRI. Statistical significance of these results was not evaluated, because this exploratory study was intended to show feasibility for evaluating patients with lung cancer who were undergoing treatment, regardless of the type of tumor or treatment. Therefore, these results provide a foundation for future clinical studies that can more robustly evaluate these initial observations.

DISCUSSION

We have established a protocol for performing retrospective respiratory gating for CEST MRI of the lung in a clinically relevant time frame of 3 minutes. Our protocol tracked respiration during the acquisition of CEST MR images, and removed the images that were acquired while the patient was not in the quiescent phase of respiration. We demonstrated that slowly incrementing the saturation frequency is a viable solution to generate CEST image contrast when a short 200-millisecond saturation pulse is required to accommodate respiration. Our retrospective respiratory-gated analysis method clearly improved the precision of MTR_{asym} measurements.

The MTR_{asym} values of liver with our respiration gated CEST MRI protocol were in good agreement with previously reported values of liver MTR_{asym} (28), whereas the results of the standard method were different from those previously reported. We also showed in phantoms and in vivo that the localization of MTR contrast improved by the iteratively pulsed CEST MRI technique with respiration gating, particularly near the interface between tissues and between air and tissue. This type of air/tissue localization is particularly relevant in the lung and liver. Our results also showed that measurement precision is not improved with our respiration-gated technique in tissues that are generally stationary during respiration. This finding indicates that retrospective respiratory gating is only needed when the tissue of interest is moving significantly during respiration.

Table 2. $\%MTR_{asym}$ of Patients With Cancer Undergoing Treatment

| Patient | Type | Treatment | Tumor Label | Mean $\%MTR_{asym}$ | |
				Before Treatment	After Treatment
1	Stage IIIB lung adenocarcinoma	60 Gy, 30 fractions	a	1.7	6.0
2	Stage IIIA Non-small cell lung carcinoma	60 Gy, 30 fractions	a	8.3	17.5
			b	3.3	11.5
3	Stage IV sarcomatoid pleural mesothelioma	40 Gy, 10 fractions and 6 cycles of Alimta/carboplatin	a	4.9	13.0
			c	0.5	1.1
		9 cycles of Navelbine	b	4.9	3.3
			d	0.5	−0.5
4	Stage IV mesothelioma	6 cycles of Alimta/carboplatin	a	−0.3	1.2

To implement our iteratively pulsed CEST MRI technique with respiration gating for clinical imaging, we initially selected a 20-mm-thick imaging section to ensure that the tissue of interest remained in the section plane during imaging. This spatial resolution is insufficient to measure small lesions <8 mm in diameter, which comprise the majority of lung lesions that are not immediately biopsied (29). To evaluate these smaller lesions, 3D imaging can be implemented through extremely rapid imaging via CAIPIRIHNA (30), segmentation of the 3D acquisition, partial k-space acquisition methods (31), or parallel imaging techniques (32, 33).

Our decision to select images with a phase shift within 1 radian aided the retention of ~30% of the images, resulting in about 140 points in each CEST spectrum. This level of spectral digitization was adequate for MTR_{asym} analyses. Although many other clinical CEST MRI research studies have shown that the MTR_{asym} parameter provides some diagnostic value, MTR_{asym} is sensitive to changes in both rNOE and APT, which can confound the interpretation of changes in MTR_{asym} (6). Because we acquire a full Z-spectrum, future studies could use a more rigorous and quantitative fitting technique, such as fitting CEST spectra with Lorentzian line shapes (26) or the Bloch–McConnell equations (20), or using machine learning techniques that analyze CEST spectra (34). These advanced analysis techniques can potentially evaluate CEST spectra with fewer points. This would allow for a narrower tolerance for the phase shift to be used, which would further reduce the effects of respiratory motion on CEST spectra and reduce the total scan time. Therefore, acquiring CEST spectra with the iteratively pulsed CEST MRI acquisition method with retrospective respiration gating may lead to multiple advantages in future studies.

REFERENCES
1. Ahmad A, Shirish G. Lung Cancer Statistics. Lung Cancer and Personalized Medicine. New York: Springer International Publishing Switzerland 2016.
2. Ohno Y, Hatabu H, Takenaka D, Adachi S, Kono M, Sugimura K. Solitary pulmonary nodules: potential role of dynamic MR imaging in management initial experience. Radiology. 2002;24:503–511.
3. Demura Y, Tsuchida T, Ishizaki T, Mizuno S, Totani Y, Ameshima S, Miyamori I, Sasak M, Yonekura Y. 18F-FDG accumulation with PET for differentiation between benign and malignant lesions in the thorax. J Nucl Med. 2003;44:540–548.
4. Cronin P, Dwamena BA, Kelly AM, Carlos RC. Solitary pulmonary nodules: meta-analytic comparison of cross-sectional imaging modalities for diagnosis of malignancy. Radiology. 2008;246:772–782.
5. Uto T, Takehara Y, Nakamura Y, Naito T, Hashimoto D, Inui N, Suda T, Nakamura G, Chida K. Higher sensitivity and specificity for diffusion-weighted imaging of malignant lung lesions without apparent diffusion coefficient quantification. Radiology. 2009;252:247–254.
6. Jones KM, Pollard AC, Pagel MD. Clinical applications of chemical exchange saturation transfer (CEST) MRI. J Magn Reson Imaging. 2017 [Epub ahead of print].
7. Sun PZ, van Zijl PC, Zhou J. Optimization of the irradiation power in chemical exchange dependent saturation transfer experiments. J Magn Reson. 2005;175:193–200.
8. Zhou J, Payen JF, Wilson DA, Traystman RJ, van Zijl PC. Using the amide proton signals of intracellular proteins and peptides to detect pH effects in MRI. Nat Med. 2003;9:1085–1090.
9. Zhou J, Zhu H, Lim M, Blair L, Quinones-Hinojosa A, Messina SA, Eberhart CG, Pomper MG, Laterra J, Barker PB, van Zijl PC, Blakely JO. Three-dimensional amide proton transfer MR imaging of gliomas: initial experience and comparison with gadolinium enhancement. J Magn Reson Imaging. 2013;38:1119–1128.
10. Togao O, Yoshiura T, Honda H, Keupp J, Hiwatashi A, Yamashita K, Kikuchi K, Suzuki Y, Suzuki SO, Iwaki T, Hata N, Mizoguchi M, Yoshimoto K, Sagiyama K, Takahashi M, Honda H. Amide proton transfer imaging of adult diffuse gliomas: correlation with histopathological grades. Neuro Oncol. 2014;16:441–448.
11. Ohno Y, Yui M, Koyama H, Yoshikawa T, Seki S, Ueno Y, Miyazaki M, Ouyang C, Sugimura K. Chemical exchange saturation transfer MRI Imaging: preliminary results for differentiation of malignant and benign thoracic lesions. Radiology. 2016;279:578–589.
12. Togao O, Kessinger CW, Huang G, Soesbe TC, Sagiyama K, Dimitrov I, Sherry DA, Gao J, Takahashi M. Characterization of lung cancer by amide proton transfer (APT) imaging: an in-vivo study in an orthotopic mouse model. PLoS One. 2013;8:e77019.
13. Hu Y, Caruthers SD, Low DA, Parikh PJ. Respiratory amplitude guised 4-dimensional magnetic resonance imaging. Int J Radiat Oncol Biol Phys. 2013;86:198–204.
14. Imara M, Yamazaki K, Shirato H, Onimaru R, Fujino M, Shimizu S, Harada T, Ogura S, Dosaka-Akita H, Miyasaka K, Nishimura M. Insertion and fixation of fiducial markers for setup and tracking of lung tumors in radiotherapy. Int J Radiat Oncol Biol Phys. 2005;63:1442–1447.
15. Kaskowitz L, Graham MV, Emami B, Haverson KJ, Rush C. Radiation therapy alone for stage I non-small cell lung cancer. Int J Radiat Oncol Biol Phys. 1993;27:517–523.
16. Cai J, Liu Y, Yin F. Extracting breathing signal using Fourier transform from cine magnetic resonance imaging. Cancer Trans Med. 2015;1:16–20.
17. Liu HH, Koch N, Stakschall G, Jacobson M, Forster K, Liao Z, Komaki R, Stevens CW. Evaluation of internal lung motion for respiratory-gated radiotherapy using MRI: Part I—correlating internal lung motion with skin fiducial motion. Int J Radiat Oncol Biol Phys. 2004;60:2004.
18. Jones KM, Randtke EA, Yoshimaru E, Howison CM, Chalasani P, Klein RR, Chambers SK, Kuo PH, Pagel MD. Clinical translation of acidosis measurements with acidoCEST MRI. Molec Biol Imaging. 2017;19:617–25.
19. Barrett KE, Barman SM, Boitano S, Brooks HL. Ganong's Review of Medical Physiology. New York: McGraw-Hill Medical Publishers 2012.
20. Woessner DE, Zhang S, Merritt ME, Sherry AD. Numerical solution of the Bloch equations provides insights into the optimum design of PARACEST agents for MRI. Magn Reson Med. 2005;53:790–799.
21. Jones CK, Polder D, Hua J, Zhu H, Hoogduin HJ, Zhou J, Luiten P, van Zijl PC. In vivo three-dimensional whole-brain pulsed steady-state chemical exchange saturation transfer at 7 T. Magn Reson Med. 2012;67:1579–1589.
22. Bojorquez JZ, Bricq S, Acquitter C, Brunotte F, Walker PM, Lalande A. What are normal relaxation times of tissues at 3T? Magn Reson Imaging. 2017;35:69–80.
23. Zhou J, Yan K, Zhu H. A simple model for understanding the origin of the amide proton transfer MRI signal in tissue. Appl Magn Reson. 2012;42:393–402.
24. Shah T, Lu L, Dell KM, Pagel MD, Griswold MA, Flask CA. CEST-FISP: a novel technique for rapid chemical exchange saturation transfer MRI at 7 T. Magn Reson Med. 2011;65:432–437.
25. Cai J, Read PW, Altes TA, Molloy JA, Brookeman JR, Sheng K. Evaluation of the reproducibility of lung motion probability distribution function (PDF) using dynamic MRI. Phys Med Biol. 2007;52:365373.
26. Liu G, Li Y, Sheth VR, Pagel MD. Imaging in vivo extracellular pH with a single PARACEST MRI contrast agent. Mol Imaging. 2012;11(1):47–57.
27. Jin T, Wang P, Zong X, Kim SG. MR imaging of the amide-proton transfer effect and the pH-insensitive nuclear Overhauser effect at 9.4 T. Magn Reson Med. 2013;69(3):760–770.

28. Chen SZ, Yuan J, Deng M, Wei J, Zhou J, Wang YX. Chemical exchange saturation transfer (CEST) MR technique for in-vivo liver imaging at 3.0 tesla. Eur Radiol. 2016;26:1792–1800.

29. Swensen SJ, Viggiano RW, Midthun DE, Müller NL, Sherrick A, Yamashita K, Naidich DP, Patz EF, Hartman TE, Muhm JR. Lung nodule enhancement at CT: multicenter study. Radiology. 2000;214:73–80.

30. Breuer FA, Blaimer M, Mueller MF, Seiberlich N, Heidemann RM, Griswold MA, Jakob PM. Controlled aliasing in volumetric parallel imaging (2D CAIPIRINHA). Magn Reson Med. 2006;55:549–56.

31. McGibney G, Smith MR, Nichols ST, Crawley A. Quantitative evaluation of several partial Fourier reconstruction algorithms used in MRI. Magn Reson Med. 1993;30:51–59.

32. Griswold MA, Jakob PM, Heidemann RM, Nittka M, Jellus V, Wang J, Kiefer B, Haase A. Generalized autocalibrating partially parallel acquisitions (GRAPPA). Magn Reson Med. 2002;47:1202–1210.

33. Pruessmann KP, Weiger M, Scheidegger MB, Boesiger P. SENSE: sensitivity encoding for fast MRI. Magn Reson Med. 1999;42:952–962.

34. DeGrandchamp JB, Acosta PH, Cárdenas-Rodríguez J. A machine-learning approach to measuring tumor pH using MRI. Music City CEST Meeting, 2017.